CONF-940412--4

Note: This is a preprint of a paper submitted for publication. Contents of this paper should not be quoted or referred to without permission of the author(s).

For publication in *Proceedings of the 39th International Society for Advanced Materials and Process Engineering (SAMPE) Symposium and Exhibition*, Anaheim, California, April 11–14, 1994

ATOMIC SCALE STRUCTURE AND CHEMISTRY OF INTERFACES BY Z-CONTRAST IMAGING AND ELECTRON ENERGY LOSS SPECTROSCOPY IN THE STEM*

M. M. McGibbon, N. D. Browning, M. F. Chisholm, and S. J. Pennycook

Solid State Division
Oak Ridge National Laboratory
Oak Ridge, Tennessee 37831-6031

---

*This research was sponsored by the Division of Materials Sciences, U.S. Department of Energy, under contract DE-AC05-84OR21400 with Martin Marietta Energy Systems, Inc.

SOLID STATE DIVISION
OAK RIDGE NATIONAL LABORATORY
Managed by
MARTIN MARIETTA ENERGY SYSTEMS, INC.
under
Contract No. DE-AC05-84OR21400
with the
U.S. DEPARTMENT OF ENERGY
Oak Ridge, Tennessee

December 1993

ATOMIC SCALE STRUCTURE AND CHEMISTRY OF INTERFACES BY Z-CONTRAST IMAGING AND ELECTRON ENERGY LOSS SPECTROSCOPY IN THE STEM

M. M. McGibbon, N. D. Browning, M.F.Chisholm and S. J. Pennycook
Solid State Division, Oak Ridge National Laboratory, Oak Ridge, TN 37831-6031. USA

ABSTRACT

The macroscopic properties of many materials are controlled by the structure and chemistry at the grain boundaries. A basic understanding of the structure-property relationship requires a technique which probes both composition and chemical bonding on an atomic scale. The high-resolution Z-contrast imaging technique in the scanning transmission electron microscope (STEM) forms an incoherent image in which changes in atomic structure and composition can be interpreted intuitively. This direct image allows the electron probe to be positioned over individual atomic columns for parallel detection electron energy loss spectroscopy (PEELS) at a spatial resolution approaching 0.22nm. The bonding information which can be obtained from the fine structure within the PEELS edges can then be used in conjunction with the Z-contrast images to determine the structure at the grain boundary. In this paper we present 3 examples of correlations between the structural, chemical and electronic properties at materials interfaces in metal-semiconductor systems, superconducting and ferroelectric materials.

KEY WORDS: Electron Microscopy, Microanalysis, Interfaces

1. INTRODUCTION

The bulk properties of many material systems are governed by the atomic structure and chemistry of internal interfaces. Determining the nature of these interfaces on an atomic scale represents a key element in the understanding of the macroscopic behavior of materials. In principal, the electron microscope provides an ideal tool for the investigation of materials at an atomic scale (1): For example, atomic resolution images of the crystal structure can be produced by a conventional transmission electron microscope (CTEM). However, the images formed in the CTEM are coherent and as such are complicated by image contrast reversals which are sensitive to operating parameters such as specimen thickness and focus. Consequently, quantitative interpretation of such images is problematical and can only be done by comparing images to simulations calculated for specific models. Accurate quantitative chemical microanalysis can be carried out in the CTEM using, for example, parallel detection electron energy loss spectroscopy and energy dispersive x-ray (EDX) microanalysis, although the spatial resolution of these analytical techniques is limited to ~10 to 20Å compared to the image resolution of 1 to 2Å in the same microscope.

The recent development of the incoherent Z-contrast imaging technique (2) using a dedicated scanning transmission electron microscope (STEM) now enables the acquisition of directly interpretable images of materials interfaces at atomic resolution. In the VG HB501 UX dedicated STEM (figure 1), the image is formed by scanning a 2.2Å probe across the specimen. The integrated output from various imaging detectors is displayed on a TV screen

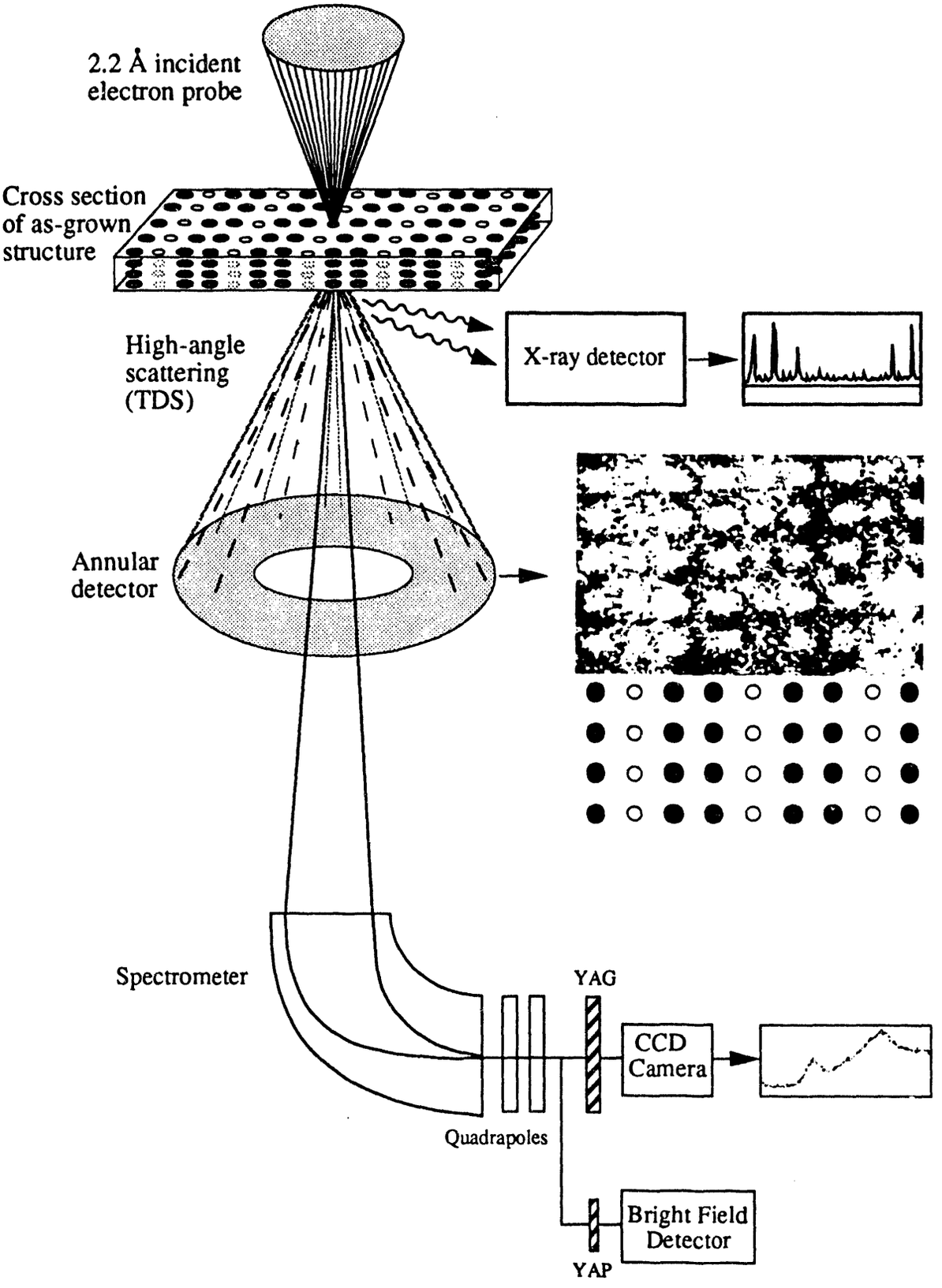

Figure 1: A schematic representation of the detector arrangement in the VG HB501 dedicated STEM. Both EDX and EELS can be performed simultaneously with Z-contrast imaging.

scanning at the same rate. The spatial resolution of the image is governed by the microscope probe size and by holding the probe stationary for microanalysis, the spatial resolution of the analytical signal can now be identical. The detector arrangement in the STEM has the added advantage of allowing the Z-contrast image to be collected simultaneously with the analytical signal (3).

2. EXPERIMENTAL TECHNIQUES

2.1 Z-Contrast Imaging In STEM, the Z-contrast signal is collected from a high angle annular detector as shown in figure 1. By collecting the component of the electron signal scattered through much larger angles (typically 75 to 150 mrad) than is acquired in normal CTEM imaging, the resultant image is dominated by thermal diffuse scattering. In this high angle regime, lateral coherence between individual columns is destroyed provided the signal is collected over a sufficiently large angular range, and coherence between atoms in the same column will be destroyed by thermal vibrations. This produces an image showing incoherent characteristics, with the resolution of the scanning probe (4). Provided the incident electron probe is smaller than the lattice spacing (for a sample oriented to a major zone axis) the resultant image will be a map of the columnar scattering intensity as shown schematically in figure 1. Furthermore, the relative intensity of scattering from each column reflects the changes in the composition on an atomic scale as shown for a $YBa_2Cu_3O_{7-\delta}$ superconductor in figure 1 where the Ba atoms show up brightest since they scatter most strongly (ie. have the highest Z value of 56). The Y atoms are also visible (Z=39) but the Cu atoms (Z=29) are barely discernible above the background intensity. Note however that Co (Z=27) shows up very brightly against Si (Z=14) as shown later, hence the term Z-contrast imaging.
For thicker samples, where beam spreading might be expected to degrade the resolution theoretical calculations (4) have shown that the spatial resolution is preserved by channeling of the electrons down the atomic columns, provided the sample is oriented on a major zone axis. Experiments have confirmed the electron channeling effect in thicker samples (~500Å) where the image merely reduces in contrast as the incident beam becomes depleted by the increasing number of scattering events.
The key aspect of this technique then is that image intensity distributions in high-resolution Z-contrast images provide a direct image of the atomic column sites which is sensitive to both structure and composition on an atomic scale (5). High resolution CTEM images do not give a direct interpretation of the atomic sites and are further complicated by reversals in image contrast through focus. In addition, as the Z-contrast signal is collected from an annular detector, the inelastic signal, which is scattered through significantly lower angles can be collected simultaneously to form an energy loss spectrum. Consequently, the high-resolution Z contrast image can be used to position the electron probe on specific atomic sites to collect electron energy loss spectra.

2.2 Core-loss Electron Energy Loss Spectroscopy When 100keV electrons pass through a specimen, a small fraction of the electrons interact inelastically with the sample losing energy in the process. By collecting these inelastically scattered electrons via a spectrometer, the resultant energy loss distribution known as the electron energy loss spectrum can be recorded. In a manner analogous to X-ray absorption, each spectrum is characteristic of the elements present in the irradiated specimen volume and can provide quantitative elemental information in this region. An example of an oxygen EELS edge for an $YBa_2Cu_3O_{7-\delta}$ superconductor is shown in figure 7.
Due to the formation of the small probe used for the Z-contrast imaging, the beam current is reduced by a factor of 50 over that which is normally available for EELS in the STEM. This reduction in the EELS signal coupled with the requirement of short acquisition times to reduce specimen drift when collecting from individual atomic columns requires a large increase in the sensitivity of the detection system. This has been carried out using a charge coupled device (CCD) parallel detection system based on a design by McMullan et al (6). The range of signal detection afforded by the CCD system means that as well as elemental quantification it is also possible to study the spectral fine structure within an edge producing information on the local bonding (7). By integrating the signal over larger energy ranges and sacrificing energy resolution in the spectrum we expect that this CCD system should be

capable of detecting, for example, single dopant atoms in the study of elemental segregation around defects at semiconductor interfaces and grain boundaries.
In order to achieve atomic resolution EELS microanalysis, the range over which the fast electron can cause a particular excitation or energy loss must be less than the inter-atomic spacing. This range decreases with increasing energy loss and can be defined by the root mean square impact parameter:

$$b_{RMS} = \frac{\hbar v \theta_{max}}{\Delta E\left[(\theta^2_{max}+\theta^2_E)\ln\left(1+\frac{\theta^2_{max}}{\theta^2_E}\right)\right]^{1/2}}$$

where E is the incident beam energy, ΔE is the energy loss ($\Delta E << E$), v the electron velocity, θ_{max} is the aperture limited cut-off angle, and $\theta_E = \Delta E/2E$.

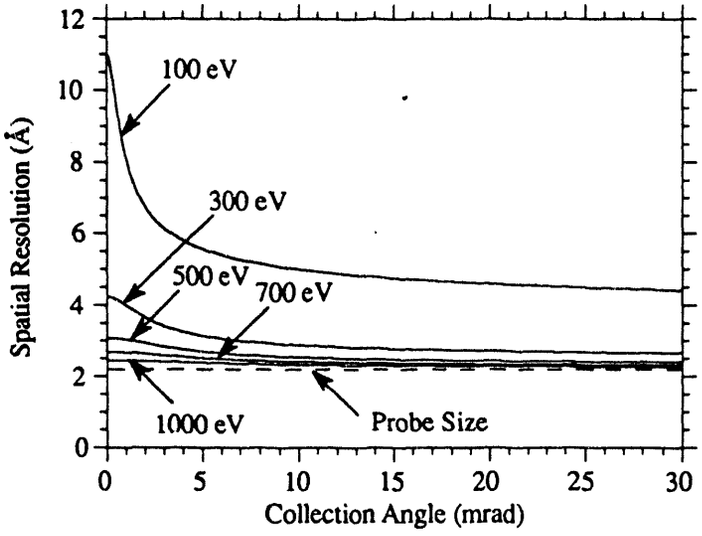

Figure 2: Spatial resolution of the EELS signal (defined as the probe size and impact parameter added together in quadrature) as a function of collection angle for various energy losses. A collection angle of 30mrad was used in this work.

Figure 2. shows the expected spatial resolution of the energy loss signal as a function of collection angle for various energy losses. We can see that for energy losses greater than ~300eV and a collection angle of 30mrad (typical in the work presented here) the impact parameter is sufficiently small that the spatial resolution of the EELS signal is dominated by the incident probe size of 2.2Å. Whether energy losses below 300eV can be considered as generated from a single atomic column depends on the inter-atomic spacing of the material under study. Note however, that since the spectrometer provides energy discrimination it is only necessary to consider the spacing between neighbouring columns containing the element in question.

3. ATOMIC RESOLUTION CHARACTERISATION OF INTERFACES

As discussed above, the experimental arrangement for STEM (figure 1) allows the Z-contrast image to be used to select an individual atomic column on which to perform EELS analysis. Although the Z-contrast image is insensitive to light elements, such as O, the image can be used to determine the structure of the material and to identify possible positions for such atoms. EELS microanalysis can then be carried out in selected areas of the image at an atomic resolution to give information on the composition and bonding of the lighter elements in the sample.

3.1 Cobalt Disilicide-Silicon Interfaces The extent to which the previous theoretical considerations of atomic resolution EELS can be applied to real interface systems is demonstrated by the following study of a $CoSi_2$-Si interface, described in more detail in (8). The spatial resolution of the EELS signal can be determined by examining the Co L_{23} edge across the interface between cobalt silicide and silicon. From the spatial resolution calculation shown in figure 2, the EELS signal of the Co L_{23} edge at an energy of 780eV and using a

30mrad collector aperture should be sufficiently localised to allow atomic resolution microanalysis across the interface.

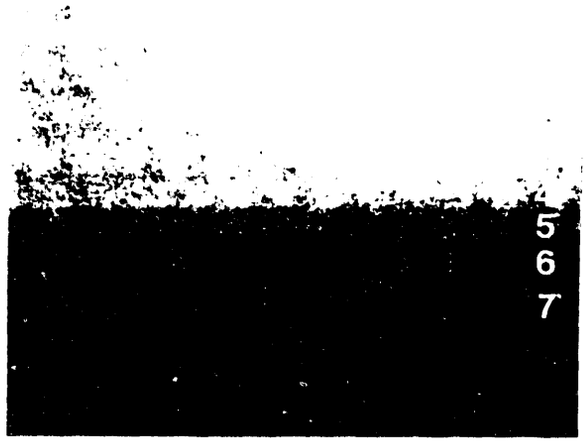

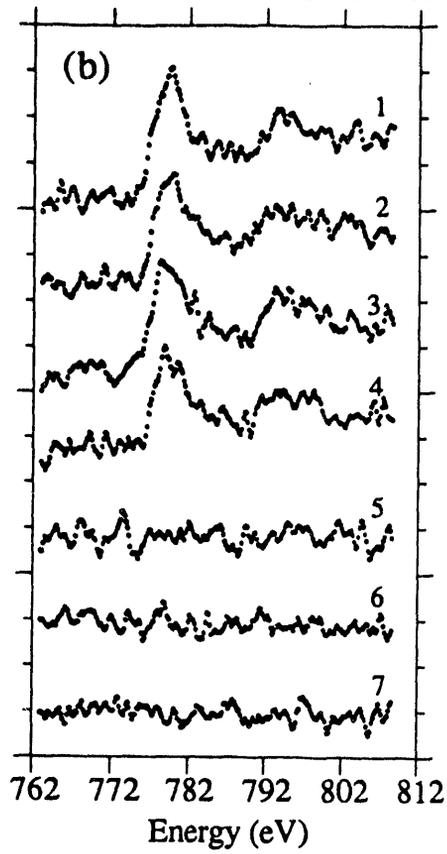

Figure 3: (a) A Z-contrast image from a {111} facet at a $CoSi_2$-Si interface which shows that the interface is atomically abrupt. (b) A series of Co L_{23} spectra collected at successive planes across the interface as indicated in the image of figure 3(a).

A buried $CoSi_2$ layer was produced by an ion implantation and annealing procedure (9), which resulted in a continuous buried $CoSi_2$ layer consisting of {001} terraces separated by occasional {111} facets. The Z-contrast image from one of the {111} facets is shown in figure 3(a) where the brighter regions correspond to the increased scattering power of the heavier Co in the $CoSi_2$. Note that the Si present in the $CoSi_2$ is not resolved and so contributes to the uniform bright background seen between the Co atoms. The image shows that the interface is atomically abrupt, changing from $CoSi_2$ to Si over a single atomic plane (10). As well as giving information on the interface structure, the Z-contrast image can also be used to position the electron probe for EELS. In order to reduce the electron dose and thus radiation damage in the sample, the EELS were acquired while scanning the probe repeatedly along a line parallel to the interface. This allows the probe to be positioned very accurately over an individual plane of atoms using an oscilloscope to display the line scan. Whilst reducing the dose incident on the sample by scanning planes of atoms, this technique retains atomic resolution in a direction perpendicular to the interface. Figure 3(b) shows a series of Co L_{23} spectra collected at successive atomic planes across the interface. From the figure it can be seen that the Co signal drops to zero over a single atomic plane across the interface in agreement with the Z-contrast image.

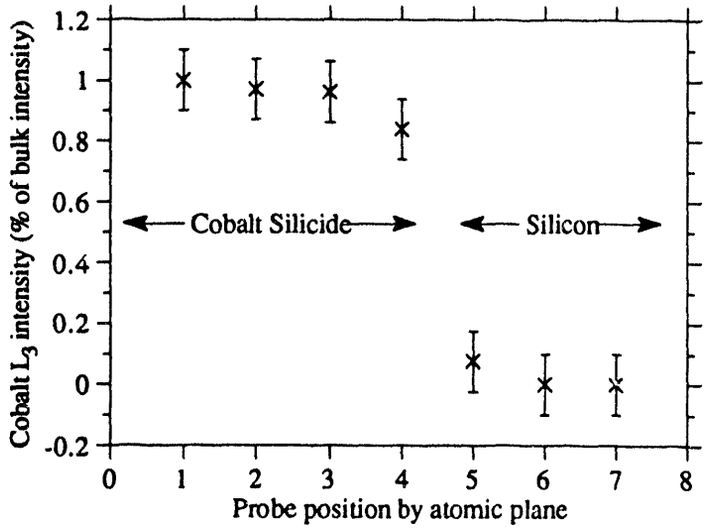

Figure 4: The normalised Co L_3 edge intensity profile across the interface shows that the Co EELS signal is atomically abrupt.

Figure 4 shows a quantitative Co concentration profile obtained by normalising each Co L_3 edge intensity to the intensity obtained from bulk $CoSi_2$ several planes away from the interface. By the definition of edge resolution, the reduction in the Co L_3 intensity from 86% to 7% across a single atomic plane demonstrates that atomic resolution analysis has been achieved across this interface using the dual technique of Z-contrast imaging and EELS. The planar separation at the interface is 2.7Å due to stacking fault visible at the first Si plane.
Figure 5(a) shows a Z-contrast image of the $CoSi_2$ {001} interface from the same sample as above. Energy loss spectra were acquired at successive planes across the interface as described above for the {111} interface and are shown in figure 5(b).

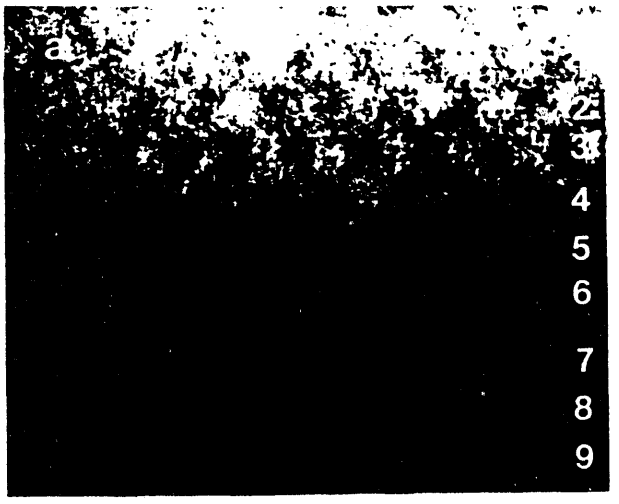

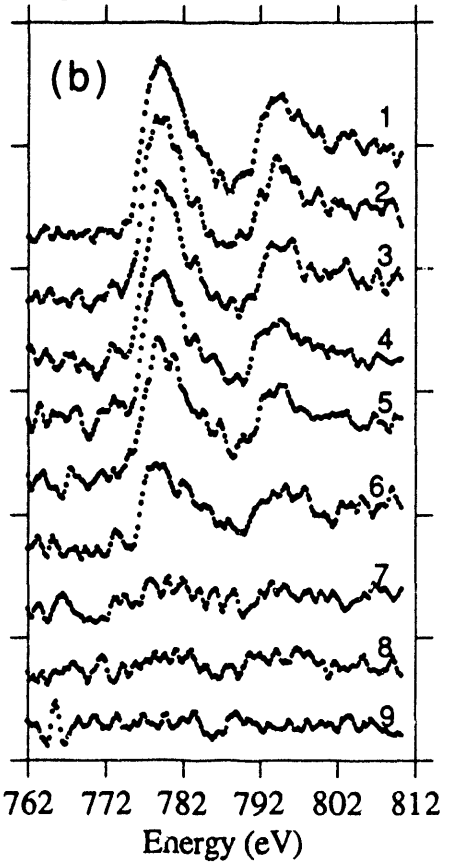

Figure 5: (a) A Z-contrast image from a {001} $CoSi_2$-Si interface which shows that the interface is not atomically abrupt. (b) A series of Co L_{23} spectra collected at successive planes across the interface as indicated in the image of figure 5(a).

Figure 6 shows the normalised Co L_3 signal plotted plane by plane across the interface. Both the image and the Co signal across the interface indicate that this interface is not atomically abrupt. The 50% intensity drop in the Co L_3 edge intensity is consistent with the 2x1 arrangement of Co atoms seen in the Z-contrast image. Note that a similar structure involving Co ordering was ruled out during a detailed high resolution study in a CTEM, since simulations did not reproduce the observed lattice shifts across the interface seen experimentally (11). From the Z-contrast image it was deduced that an unexpectedly large interface expansion accompanied the Co ordering, consistent with the observed lattice shifts (12).

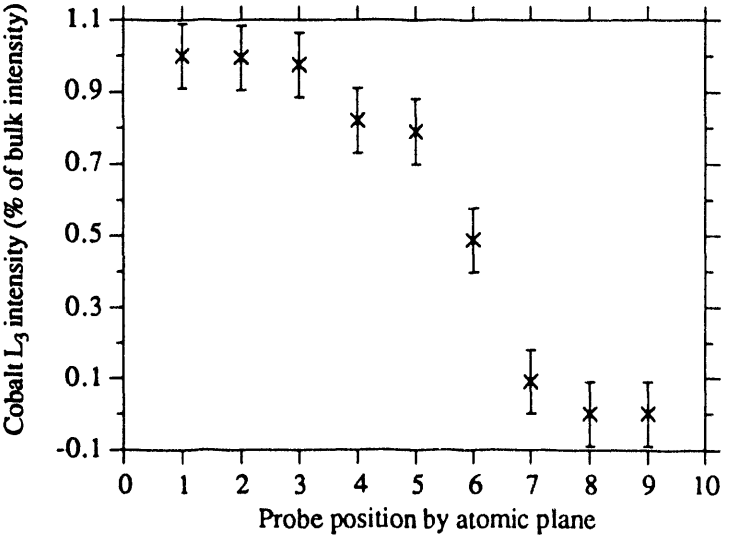

Figure 6: The normalised Co L_3 edge intensity profile across the interface. The 50% reduction in the Co signal at the interface is consistent with the 2x1 arrangement of Co atoms seen in the Z-contrast image of figure 5(a).

3.2 Hole Depletion at $YBa_2Cu_3O_{7-\delta}$ High Angle Grain Boundaries Having proven the atomic resolution capabilities of the EELS signal we can now apply the technique to another important system in which compositional variations on an atomic level can profoundly affect materials properties, namely hole depletion in superconductor grain boundaries (13). Holes in the oxygen 2p conduction band which are thought to be responsible for the superconducting properties produce a pre-edge feature in the EELS O edge as electrons are excited from the O core level to fill these holes (14, 15). Figure 7 shows a comparison of the EELS O edges for a fully-oxygenated, superconducting sample and a non-oxygenated sample which does not possess holes in the O 2p valence band. Note that the intensity of the pre-edge peak is zero in the latter. Thus, we have a feature in the fine structure which is directly linked to the superconducting properties allowing us to measure, for example, the hole depletion across a grain boundary, where the critical current is likely to be significantly reduced from that found within the grains.

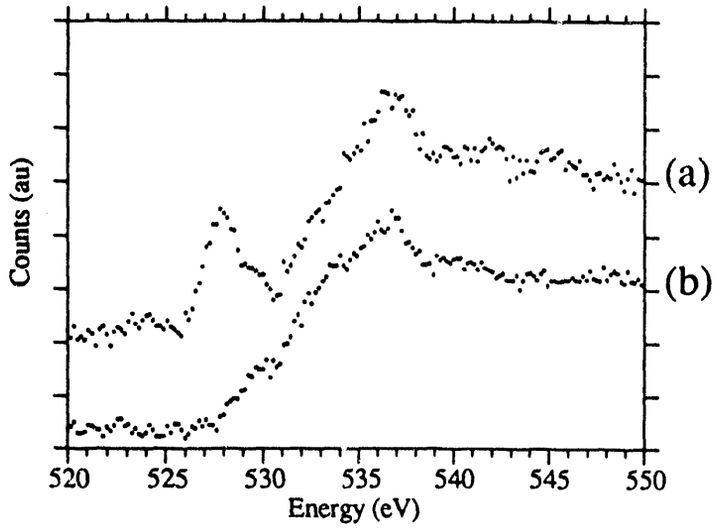

Figure 7: O K-edge spectra from a $YBa_2Cu_3O_{7-\delta}$ superconductor. (a) The pre-edge feature in the doped material (δ=0) corresponds to transitions of electrons from the core level to holes in the O 2p valence band. (b) Note the absence of the pre-edge feature for undoped material (δ~1) where there are no holes in the O 2p valence bands.

Figure 8 shows a Z-contrast image of a 29 degree asymmetric tilt boundary from polycrystalline $YBa_2Cu_3O_{7-\delta}$ prepared by laser ablation on an yttria-stabilised-zirconia (YSZ) substrate (16). The specimen is oriented with the c-axis perpendicular to the plane of the photograph and therefore the bright fringe separation corresponds to the 3.8Å separation of mixed Ba/Y columns in the ab-plane. The darker region visible at the grain boundary indicates strain and/or amorphous regions along the grain boundary.

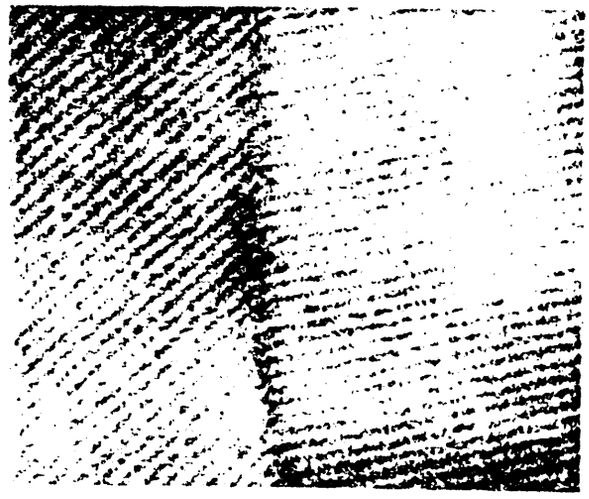

Figure 8: Z-contrast image of an asymmetric 29 degree grain boundary in polycrystalline $YBa_2Cu_3O_{7-\delta}$.

A series of oxygen K-edge spectra were collected at 8Å intervals across this interface, again using line scans parallel to the interface to reduce radiation damage in the sample. By collecting two 5s spectra at each point, it was possible to determine that there was no beam damage during these short spectrum acquisition times, enabling spectra to be added together to improve statistical accuracy. The spectra are shown in figure 9. To emphasize changes in the pre-edge feature only every second spectrum is shown giving a 16Å separation between spectra. The pre-edge feature at 528.5eV is clearly seen to diminish in the region of the boundary and is virtually zero at the grain boundary itself. These changes were quantified using normalised gaussian functions to model the main features of the spectrum (13) resulting

in a profile of hole depletion across the boundary, as shown in figure 10. The figure clearly shows a significant hole depletion zone over a range 50 to 60Å either side of the grain boundary. This is a significantly larger region than the amorphous/strained regions at the grain boundary in figure 8 (~ 5 to 10Å) suggesting that the electronic structure is disrupted over a significantly larger region than the disruption in the crystal structure seen in the Z-contrast image.

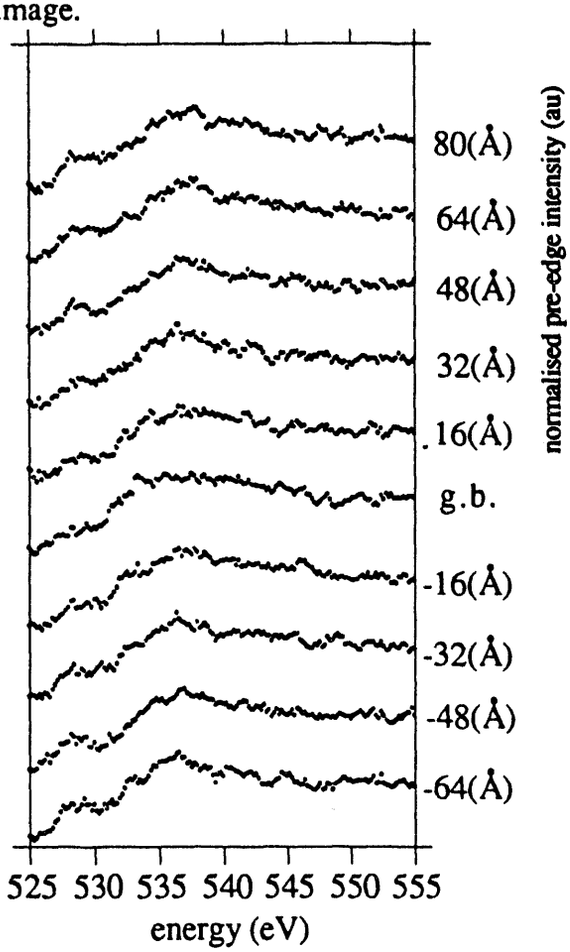

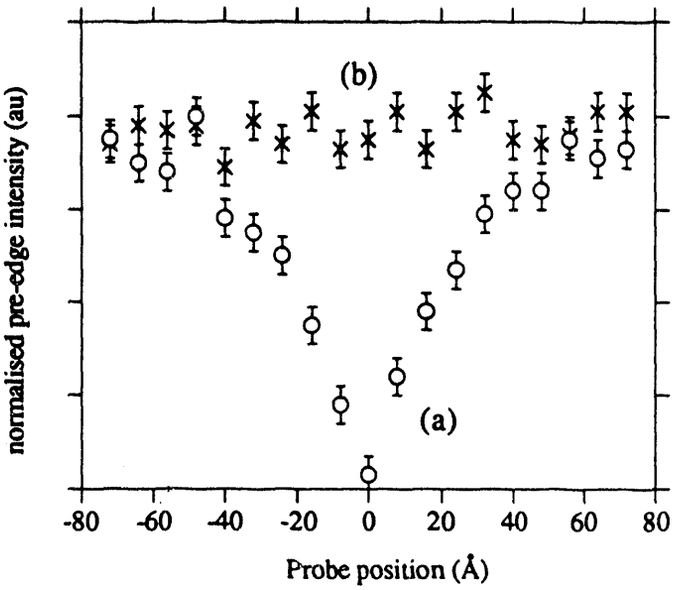

Figure 10:(a) Hole depletion profile across the asymmetric grain boundary calculated by fitting normalised gaussians to the pre-edge peak. The hole depletion profile for the symmetric grain boundary (b) is also shown for comparison.

Figure 9: O K-edge spectra recorded at 16Å intervals across the grain boundary shown in figure 8. There is a reduction in the pre-edge peak intensity (at 528eV) as the probe is traced across the boundary.

Figure 11 shows a high resolution Z-contrast image of a symmetric 36 degree tilt boundary from the same sample as the asymmetric tilt boundary discussed above. The image was obtained under the same conditions as figure 8 with the bright fringe separation corresponding to the 3.8Å separation of the Ba/Y mixed columns as before. This grain boundary is nearly a mirror plane and is free from the amorphous phase or strained region observed in the asymmetric tilt boundary. The reason that one grain shows much brighter than the other is most likely due to a small specimen tilt.

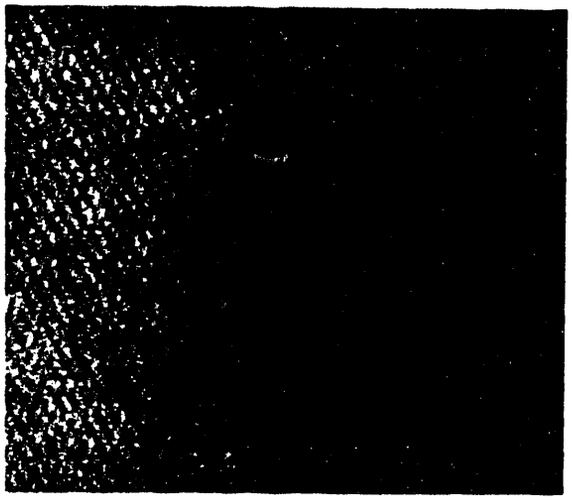

Figure 11: Z-contrast image of a symmetric 36 degree grain boundary in polycrystalline $YBa_2Cu_3O_{7-\delta}$

As for the previous example, a series of EELS spectra were acquired in line scan mode across the boundary at 8Å intervals. However, the spectra shown in figure 12 show no significant decrease in the pre-edge peak across the grain boundary. The profile of the hole depletion across the symmetric boundary is shown in figure 10 for comparison with the asymmetric boundary. To within the experimental error the symmetric boundary shows no evidence of any hole depletion zone at this boundary.

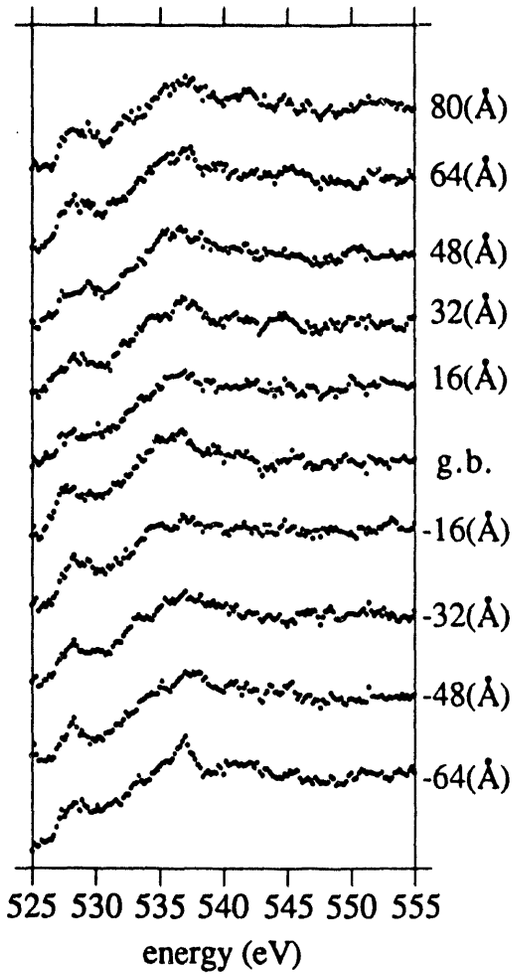

Figure 12: O K-edge spectra recorded at 16Å intervals across the grain boundary shown in figure 11. Within experimental errors there is no significant reduction in the pre-edge peak intensity (at 528eV) as the probe is traced across the boundary.

The combination of Z-contrast imaging and parallel EELS allows the study of the electronic structure in grain boundaries on a scale previously unattainable. The occurrence of a hole depletion zone as a function of structural disorder suggests that there is a strong link between the structure at the grain boundary and the associated hole depletion. This provides the first clear microscopic evidence that not all high-angle grain boundaries act as weak links, as proposed by Babcock et al (17)

3.3 Grain Boundaries in a $SrTiO_3$ Bicrystal. $SrTiO_3$ is an important ferroelectric material whose properties depend on the structure at grain boundaries. Figure 13 shows a Z-contrast image from a 25° tilt boundary in a $SrTiO_3$ bicrystal. The specimen was oriented in the <100> direction with a common boundary plane of (920) in the perovskite structure of $SrTiO_3$. The brighter regions in the image correspond to the strong scattering power of the heavier Sr columns (which have a spacing of 3.9Å in the <100> direction) whilst the lighter Ti columns are just discernible above the background. Although the position of the Sr and Ti columns can be clearly located, it is not possible to determine the O structure at the grain boundary from the Z-contrast image alone. However, we can use the fine structure in the EELS edges to investigate the nature of the O and Ti bonding at the grain boundary.

Figure 14 shows a series of Ti spectra acquired at 4Å intervals across a $SrTiO_3$ grain boundary as described for the $CoSi_2$ spectra in section 3.1. The intensity of the sharp peaks, known as white lines, found at the onsets of the Ti L_2 and Ti L_3 absorption edges reflects the filling of the d-states in transition metals such as Ti (18,19). After normalising the white line intensity relative to the trailing background any changes in this normalised intensity will reflect changes in the d-states themselves caused by a change in the local atomic environment of the Ti atoms.

Figure 13: Z-contrast image of a 25° grain boundary in a $SrTiO_3$ bicrystal.

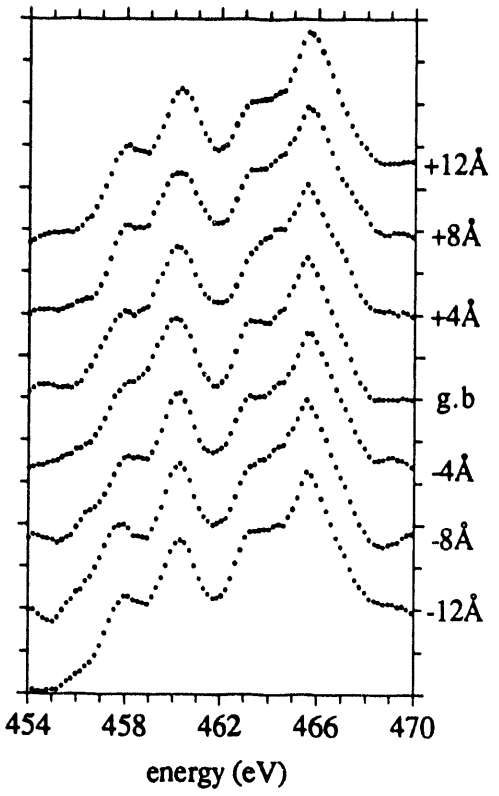

Figure 14: Ti L_{23} spectra acquired at 4Å intervals across a 25° $SrTiO_3$ grain boundary.

In the bulk $SrTiO_3$, the Ti atoms are octahedrally coordinated to O and have a valency of 4+. Figure 15(a) shows the normalised white line intensity across the grain boundary measured from the Ti spectra of figure 14. Within the experimental limits the normalised white line intensity remains constant across the grain boundary indicating that the local atomic environment is similar at the grain boundary and that Ti is octahedrally coordinated to O throughout the sample.

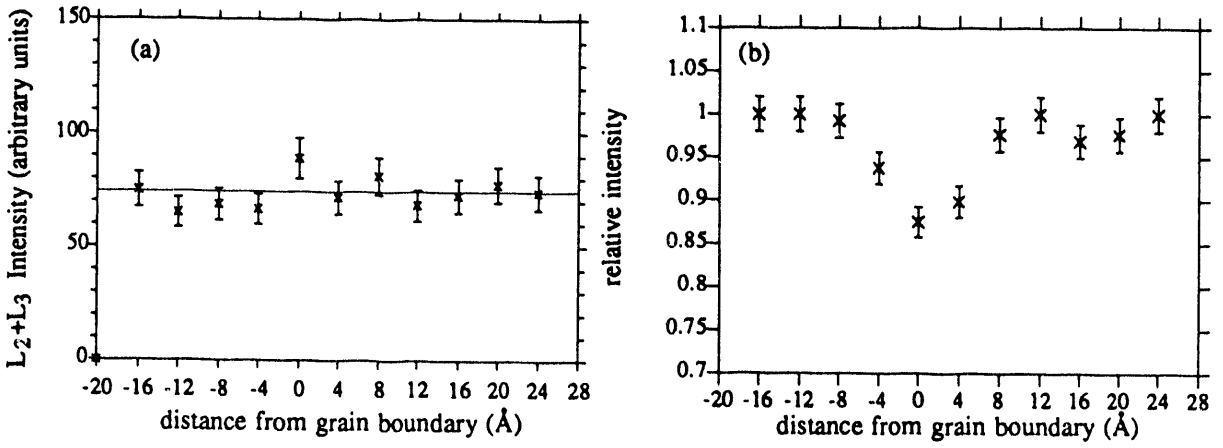

Figure 15: (a) A constant value for the Ti L_{23} white line intensity across the grain boundary suggests that the Ti coordination remains the same throughout the sample. (b) A decrease in the normalised π^* intensity profile suggests that the Ti-O bonds have been distorted at the grain boundary.

In figure 14 however, changes in the fine structure of the Ti edge, in particular a decrease in intensity of the first peak, were observed across the grain boundary. Molecular orbital calculations assign the first peak in both the Ti L_3 and O K edges to a π^* transition, whilst the second peak in both edges is assigned to a σ^* transition. The decrease in π^* intensity across the grain boundary was quantified by fitting gaussian profiles to the spectra and the results are shown in figure 15(b). The ~15% decrease in the intensity of the π^* transitions at the grain boundary relative to those in the bulk material suggest that the Ti-O bonds, which gives rise to the π^* transitions, are affected by the grain boundary. Therefore, although the Ti atoms remain octahedrally coordinated to O at the grain boundary the Ti-O bonds themselves have become distorted across the boundary.

A series of O spectra acquired across a second grain boundary region (figure 16) show similar changes in the fine structure of the O EELS edge. From the figure, it is clear that there is an increase in the intensity of the second peak (which corresponds to a σ^* transition) relative to the π^* peak. This is further evidence of the disruption of the linear coordination of the Ti - O bond at the grain boundary.

Using a combination of the structural information obtained from the Z-contrast image and the bonding information obtained from the PEELS it is possible to determine the likely structure at the grain boundary, purely from experimental data. The boundary structure calculated for this 25° tilt boundary is shown in figure 17. The disruption of the Ti-O linear coordination at the grain boundary can be clearly seen in this boundary reconstruction. The width of the grain boundary region in the reconstruction is ~8Å which is consistent with the Ti and O PEELS data and also reflects the extent of strain contrast seen in the Z-contrast image of figure 13.

Although the disruption of the linear coordination of the Ti-O bonds at the grain boundary in $SrTiO_3$ is perhaps not surprising the fact that this result can be directly observed on an atomic scale presents new and exciting possibilities for the study of grain boundaries.

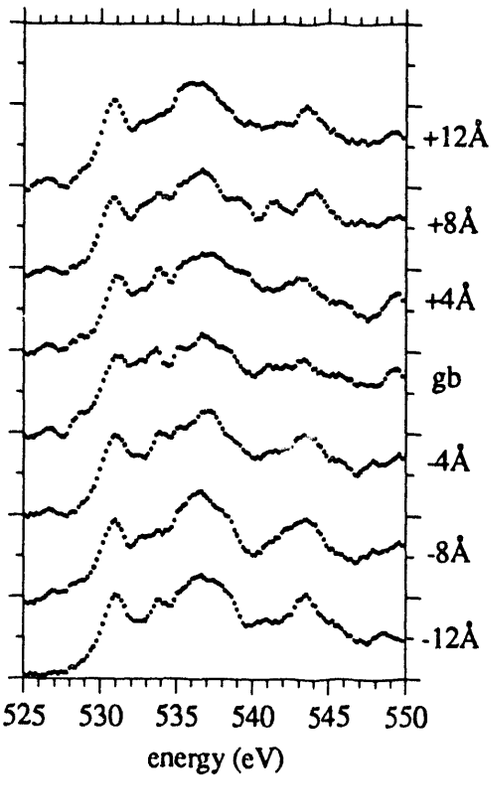

Figure 16: O K spectra acquired at 4Å intervals across a 25° $SrTiO_3$ grain boundary.

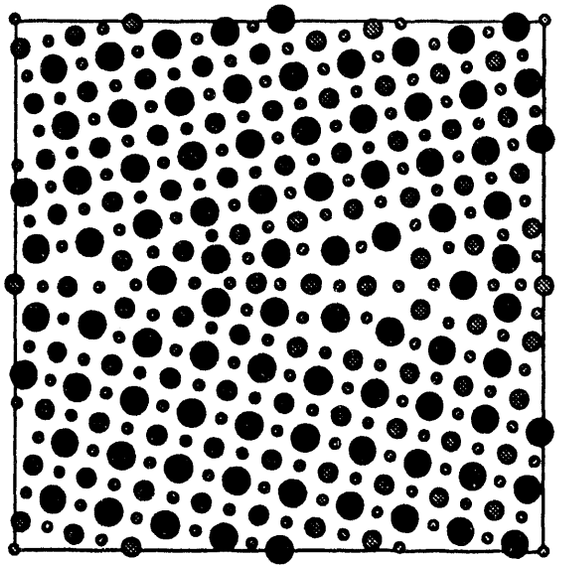

Figure 17: Boundary structure for a 25° $SrTiO_3$ grain boundary calculated using the structural information in the Z-contrast image and the bonding information in the O and Ti EELS edges.

CONCLUSIONS

Using the dual technique of Z-contrast imaging and parallel-detection EELS we have probed the interface/grain boundary structure of a number of technologically important materials on an atomic scale. In the study of a $CoSi_2$-Si interface we have demonstrated atomic resolution microanalysis across two different interfaces and by correlating Z-contrast imaging and EELS data we have confirmed the existence of an interfacial structure previously unforeseen. The atomic scale EELS results from high angle grain boundaries in $YBa_2Cu_3O_{7-\delta}$ superconductors allow the measurement of the electronic structure of the grain boundary on a scale previously unattainable. These results suggest a strong correlation between structure at the grain boundary and the associated hole depletion across the grain boundary. In the ferroelectric material $SrTiO_3$ both Z-contrast imaging and EELS analysis have been used to probe the structure and bonding at the grain boundary on an atomic scale. From these experimental results alone, a model for the grain boundary structure was determined.
The above results demonstrate that Z-contrast imaging in conjunction with EELS can be used to probe both the structural and chemical environment at grain boundaries on an atomic level. This presents new and exciting possibilities in the understanding of the relationship between interface structures and the macroscopic properties exhibited by these materials.

REFERENCES

(1) L.M.Brown, J.Phys.F, 11, 1 (1981)
(2) S.J. Pennycook and D.E. Jesson, Physical Review Letters, 64, 938, (1990)
(3) A.V. Crewe, J. Wall and J. Langmore, Science, 168, 1338, (1970)
(4) S.J. Pennycook and D.E. Jesson, Ultramicroscopy, 37, 14, (1991)
(5) S.J. Pennycook, Annu. Rev. Mater. Sci., 22, 171, (1992)
(6) D.McMullan et al, Institute of Physics Conference Series 98, 55, (1990)
(7) N.D.Browning and S.J.Pennycook, Microbeam Analysis, 2, 81, (1993)
(8) N.D.Browning et al, Nature , 366, 143 (1993)
(9) A.Schuppen et al, Materials Science and Engineering, B12, 157 (1992)
(10) M.F.Chisholm et al, Appl.Phys.letters, (submitted to)
(11) A.F. de Jong and C.W.T.Bulle-Lieuwma, Phil Mag A, 62, 183, (1990)
(12) M.F.Chisholm et al, Appl.Phys.letters, (submitted to)
(13) N.D.Browning et al, Physica C, 212, 185, (1993)
(14) N.Nucker et at, Phys.Rev B, 39, 6619, (1989)
(15) N.D.Browning, J.Yuan and L.M.Brown, Physica C, 202, 12, (1992)
(16) D.P.Norton et al, J Appl Phys, 68, 223, (1990)
(17) S.E.Babcock et al, Nature, 347, 167, (1990)
(18) M.DeCrescenzi et al, Phys Rev B, 39, 5520 (1989)
(19) D.H.Pearson, C.C.Ahn and B.Fultz, Phys. Rev B, 47, 8471 (1993)

END

DATE FILMED

4/7/94